PHYSICAL REVIEW C VOLUME 32, NUMBER 1 JULY 1985

Coincident neutron-proton emission from proton bombardment of ^{87}Sr and ^{91}Zr

J. C. Dousse
Physics Department, University of Fribourg, 1700 Fribourg, Switzerland
and Los Alamos National Laboratory, Los Alamos, New Mexico 87545

E. D. Arthur, D. M. Drake, J. Gursky, J. D. Moses, N. Stein, and J. W. Sunier
Los Alamos National Laboratory, Los Alamos, New Mexico 87545

(Received 2 November 1984)

Cross sections were measured for the reactions $^{87}\mathrm{Sr}+\mathrm{p}\rightarrow{}^{86}\mathrm{Sr}+\mathrm{pn}$ and $^{91}\mathrm{Zr}+\mathrm{p}\rightarrow{}^{90}\mathrm{Zr}+\mathrm{pn}$ using two time-of-flight neutron detectors located at 65° and 100°, and a charged particle telescope at 135°. Results are presented for several incident energies from 14.0 to 17.6 MeV. They are compared with Hauser-Feshbach calculations, with which they substantially agree.

I. INTRODUCTION

Recent measurements[1–4] of proton spectra produced by 14-MeV neutrons incident on nuclei ranging from ^{27}Al to ^{93}Nb have shown large variations in proton emission rates which arise when (n,np) and (n,pn) reactions become important. This occurs for target nuclei for which proton emission is allowed over a region of excitation energy where neutron emission is energetically forbidden. Such "proton windows" are especially prevalent in the mass 90 region where both proton and neutron shell closures occur. For example, the total proton emission cross section for neutrons incident on ^{92}Mo reported in Ref. 4 is almost an order of magnitude larger than for other molybdenum isotopes; the cause is enhanced proton emission from ^{92}Mo due to the 5.22 MeV difference between proton and neutron binding energies. This effect is also observed in measurements[5] of the total (n,np) and (n,pn) cross sections of 14-MeV neutrons on the proton rich and unstable isotope ^{88}Zr, where similar binding energy differences occur.

Reactions populating proton windows can test the sub-Coulomb barrier behavior of the proton optical model, complementing low-energy (p,n) cross section data.[6,7] In addition, they may constrain theoretical calculations sensitive to the competition between gamma-ray and proton emission. The effects of (n,np) reactions are largest at incident neutron energies close to the (n,2n) threshold, but the limited intensity of present low energy neutron sources restricts our ability to perform these measurements directly. In some cases, however, they can be simulated by charged particle induced reactions populating the same compound systems that the neutrons would excite. In an earlier experiment,[8] proton yields following the reactions ^{90,91}Zr(t,α), intended to simulate the reactions of 14 MeV deuterons on ^{88,89}Y, have been measured and analyzed; fits to the data are poor in detail. Proton induced reactions should simulate neutron reactions better, since they can excite the compound nucleus into nearly the same condition as a neutron reaction. For example, a proton of 16.7 MeV incident on ^{87}Sr produces ^{88}Y at the same excitation energy as would a 14 MeV neutron on ^{87}Y. The angular momentum at grazing incidence for the proton and neutron are the same to within one unit, so that roughly the same compound nuclear states are populated in the two reactions if the target spins are similar.

We have measured (p,np + pn) reactions populating neutron-deficient nuclei around mass 90. The targets chosen were ^{87}Sr and ^{91}Zr because the ^{87}Y and ^{91}Nb compound systems populated by the (p,n) reaction have proton separation energies that are 6.06 and 6.89 MeV less than neutron separation energies. Because of these large proton windows, we expect significant contributions from (p,np) reactions. The proton window for ^{87}Y is illustrated in Fig. 1.

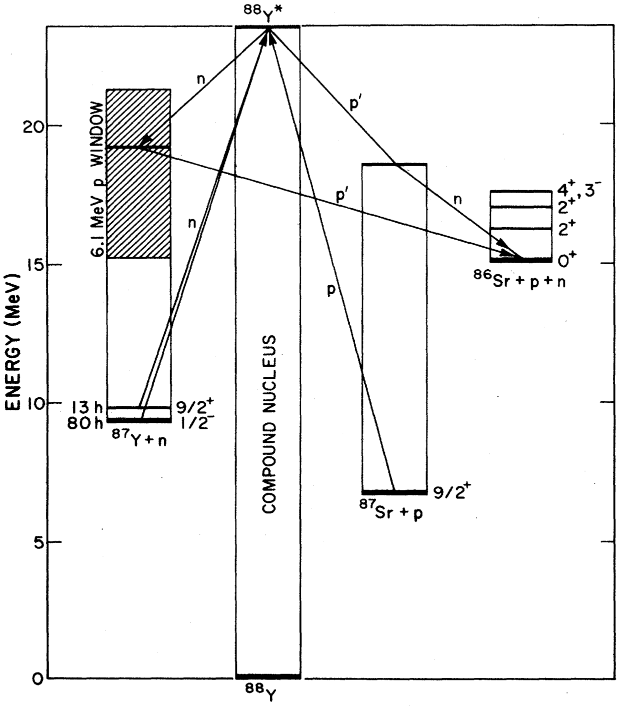

FIG. 1. Energy-isotope diagram for the production and decay of ^{88}Y*, from 16.7 MeV protons incident on ^{87}Sr, illustrating the existence of a substantial proton window in ^{87}Y.

The following sections describe our measurements of ^{87}Sr(p,pn + np) and ^{91}Zr(p,pn + np) cross sections, as well as population of discrete levels reached in the residual ^{86}Sr and ^{90}Zr nuclei via these processes. The data are then compared with theoretical predictions based on a combined multistage Hauser-Feshbach preequilibrium formalism.

II. EXPERIMENTAL METHOD

Targets of ^{91}Zr, ^{87}Sr, and ^{13}C were bombarded by protons of several energies between 14.0 and 17.6 MeV at the Tandem Van de Graaff of the Los Alamos Ion Beam Facility. The emission of both a neutron and a proton from the excited compound nucleus was detected by requiring a coincidence between the two, using the experimental arrangement shown in Fig. 2. The beam intensity varied from 15 to 50 nA and was monitored by a Faraday cup and current integrator. Several different targets of ^{91}Zr and ^{87}Sr (from 180 to 600 μg/cm^2 thick) were used during the experiment. Most of the ^{87}Sr targets were evaporated onto natural carbon backings. Oxygen contamination was kept to a minimum by transferring the targets to the scattering chamber in vacuum. Target thicknesses were measured in separate experiments using either alpha-particle energy loss, Rutherford scattering of protons at 5 MeV, comparison to targets of known thickness by elastic scattering of protons, or a combination of these techniques. The ^{13}C data were used to correct for the ^{13}C(p,pn)^{12}C reaction which occurs in the carbon backing of ^{87}Sr targets. Because the ^{13}C isotopic abundance is only 1.1%, the corrections were small. This same reaction on the main contaminants, ^{16}O and ^{12}C, does not occur because of the higher neutron separation energies.

The proton counter was a ΔE-E telescope consisting of a 30 micron silicon transmission detector for the energy-loss signal, followed by a 2000 micron E detector. The telescope enabled us to distinguish between charged particles from protons to alpha particles; fewer than 1% of the charged particles at 135° were alphas, while deuterons and tritons were negligible. The threshold on proton events was set at 1.8 MeV; a typical proton spectrum is shown in Fig. 3. The proton counter subtended a solid angle of 37 msr.

Two liquid scintillator neutron detectors using 7.6 cm-thick by 10.2 cm-diameter cylindrical cells filled with NE213 and mounted on RCA-8855 photomultipliers were located on opposite sides of the beam about 1.3 m from the target, at 65° and 100°. These scintillators were surrounded by large shields of lead and borated polyethylene to suppress gamma-ray and neutron backgrounds. Pulse shape discrimination (PSD) was used to separate neutrons from γ rays. Figure 4 shows a two-dimensional spectrum generated by plotting the time difference between the leading edge and the zero-crossover of the pulse in the neutron counter versus its pulse height. A clear separation is evident for the larger pulse heights. The low pulse height cutoff for the neutron counters was set at $\frac{1}{10}$ the Compton edge of the 667 keV γ ray of ^{137}Cs. This corresponds to a neutron threshold near 0.4 MeV.[9] Because the efficiency near threshold is rather uncertain, our results omit neutrons with energies below 0.6 MeV. The efficiency of the neutron detectors was measured using a pulsed beam of protons, a tritium target of known thickness, and the cross section of Drosg.[10] Calculated efficiencies that included double scattering effects agreed with the measurements to within the statistical precision of the measurement (see Fig. 5). The proton counter provided zero-

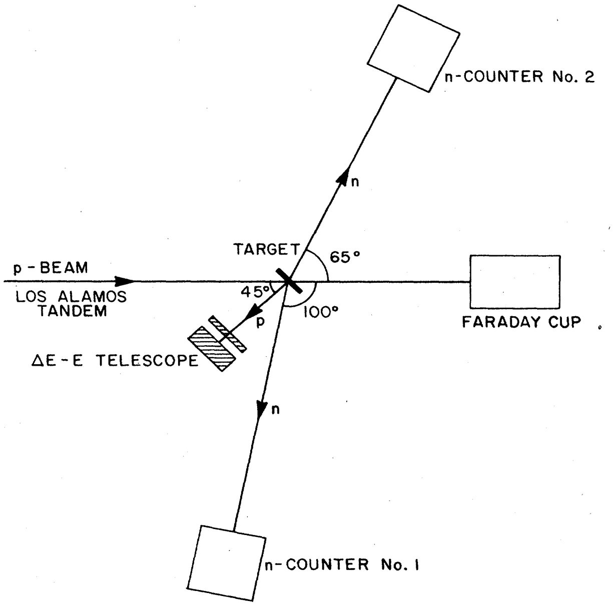

FIG. 2. Experimental arrangement.

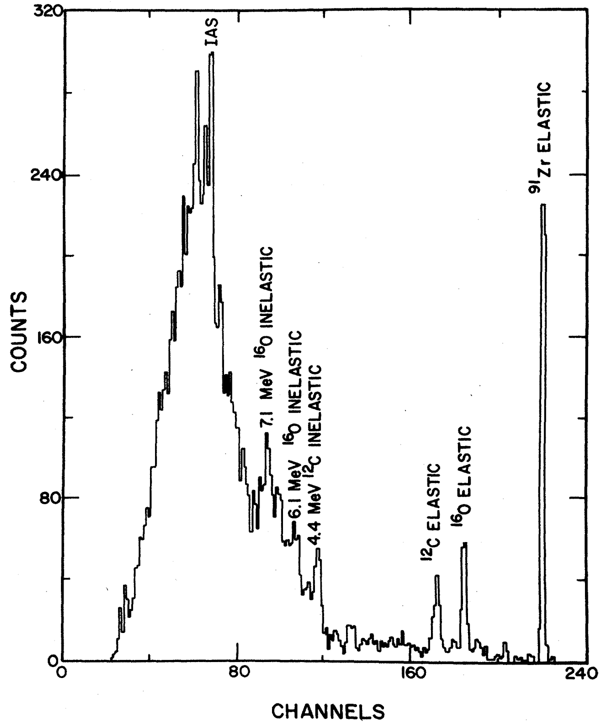

FIG. 3. Total proton spectrum of ^{91}Zr(p,p′) at 16.0 MeV (monitor spectrum).

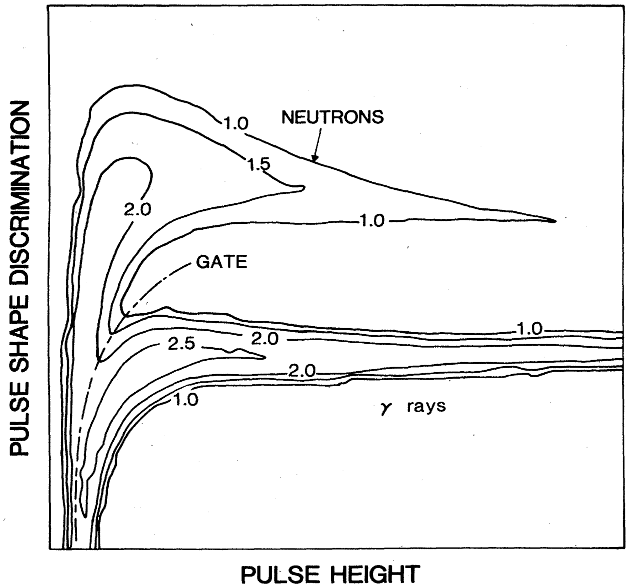

FIG. 4. Neutron-gamma pulse shape discrimination. Contour plot of the time difference between the leading edge and the zero crossover of the pulse in the neutron detector versus the pulse height. The scale of the contour levels is logarithmic. The two-dimensional gate allows the n,γ separation down to very low pulse height.

time signals for the neutron time-of-flight measurements.

Neutron-proton coincidence data were recorded event-by-event on magnetic tape with five parameters for each event. Either neutron detector provided pulse height, time of flight, and PSD signals, while the proton counter provided ΔE and E pulse heights for the charged particles. A typical two-dimensional spectrum of neutron-proton coincidences is shown in Fig. 6 for the ^{91}Zr target. The neutron energy is plotted along the y axis and the proton energy along the x axis. In all of the two-dimensional spectra, gates can be set and areas within the gates can be projected as needed by the data analysis. Thus proton and neutron spectra are obtained by projecting the two-dimensional spectra onto the x or y axes.

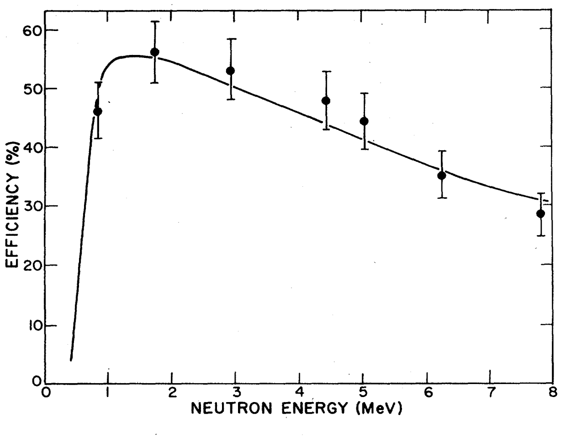

FIG. 5. Measured efficiency response of a neutron counter. The solid line is the calculated response.

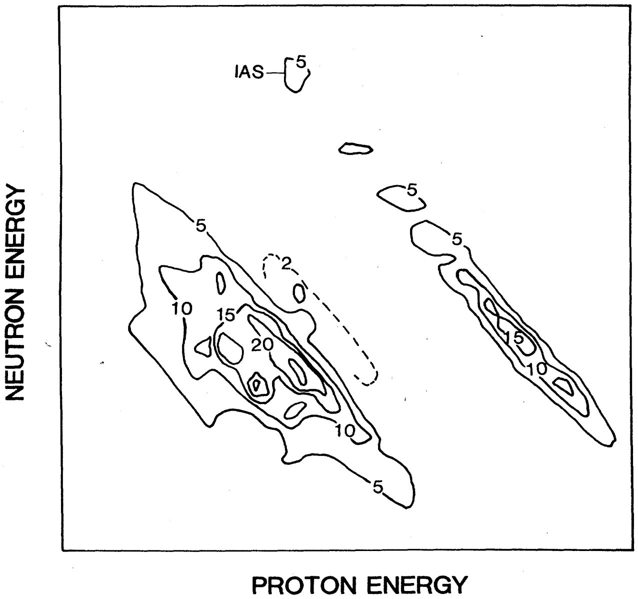

FIG. 6. Contour plot of neutron energy versus coincident proton energy for the reaction $^{91}\mathrm{Zr}+\mathrm{p}\rightarrow{}^{90}\mathrm{Zr}+\mathrm{p}+\mathrm{n}$ at 16.0 MeV incident energy. The band at right corresponds to the (p,pn + np) reactions leading to the ground state of ^{90}Zr. The other bands show population of ^{90}Zr excited states. The group marked IAS originates from the population, by the (p,n) reaction, of the ground state analog of ^{91}Zr in ^{91}Nb, and its subsequent proton decay to the ^{90}Zr ground state.

III. DATA ANALYSIS

The data were analyzed by the following procedure:

(1) Filters were set to select neutrons from the PSD spectrum and protons from the ΔE-E spectrum.

(2) Filtered events were sorted to produce two-dimensional neutron time-of-flight versus proton-energy spectra for each neutron counter.

(3) The chance coincidence background for the channels of interest was determined by examining the counts that appeared in regions of the two-dimensional spectra where no true coincidences were expected. An averaged accidental background was then subtracted [see Figs. 7(a) and (b)].

(4) The data were corrected for the efficiency of the neutron counters according to the curve shown in Fig. 5.

(5) The neutron time-of-flight axes on the two-dimensional plots were converted to neutron energy, resulting in straight parallel bands corresponding to the final states in ^{86}Sr or ^{90}Zr as shown in Fig. 6.

(6) The converted two-dimensional spectra were projected onto axes perpendicular to the parallel bands resulting in one-dimensional spectra of the final nuclei ^{86}Sr or ^{90}Zr (see Figs. 8 and 9). The counts in each final state represent the combination of both competing mechanisms; that in which the proton is emitted first and the neutron second, and that in which they are emitted in the reverse order.

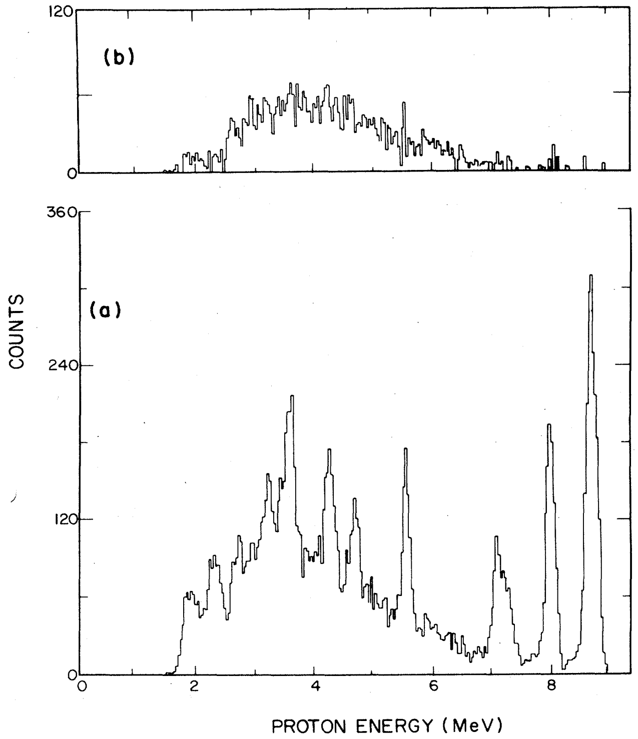

FIG. 7. Projection of the neutron time of flight versus proton-energy plot on the proton-energy axis for the reaction $^{87}\mathrm{Sr}+\mathrm{p}\rightarrow{}^{86}\mathrm{Sr}+\mathrm{p}+\mathrm{n}$ at 16.7 MeV: (a) before background subtraction, (b) after background subtraction. This particular target was strongly oxidized leading to the large contaminant peaks before background subtraction.

(7) For each final state populated in ^{86}Sr and ^{90}Zr, proton and neutron spectra can be generated by projecting the counts in each parallel band onto the proton or neutron energy axis. Such a proton spectrum is shown in Fig. 10 for various final states in ^{90}Zr. It is not possible to distinguish in these spectra those protons from the first step ^{91}Zr(p,p) followed by neutron emission compared with the second step proton emission following the ^{91}Zr(p,n)^{91}Nb reaction. The relative cross section for each final state populated by the (p,pn + np) reactions may be obtained by summing each spectrum of Fig. 10 or from the area under each peak in Figs. 8 and 9. In fact, a peak-fitting procedure was used to extract relative cross sections.

Counts from the (p,pn) reaction on the contaminant ^{13}C (arising mainly from the natural carbon backing of the ^{87}Sr targets) were subtracted, based on separate runs with a ^{13}C target. This correction amounted to a few percent at most.

The differential cross section for the (p,pn + np) reaction is given by

$$\frac{d\sigma}{d\Omega_{\mathrm{pn+np}}}=\frac{N_{\mathrm{pn+np}}}{N_{\mathrm{el}}}\frac{4\pi}{\Omega_{\mathrm{n}}}\frac{d\sigma}{d\Omega_{\mathrm{el}}} .$$

In the above equation, $N_{\mathrm{pn+np}}$ is the total number of counts in a final state corrected for the neutron attenua-

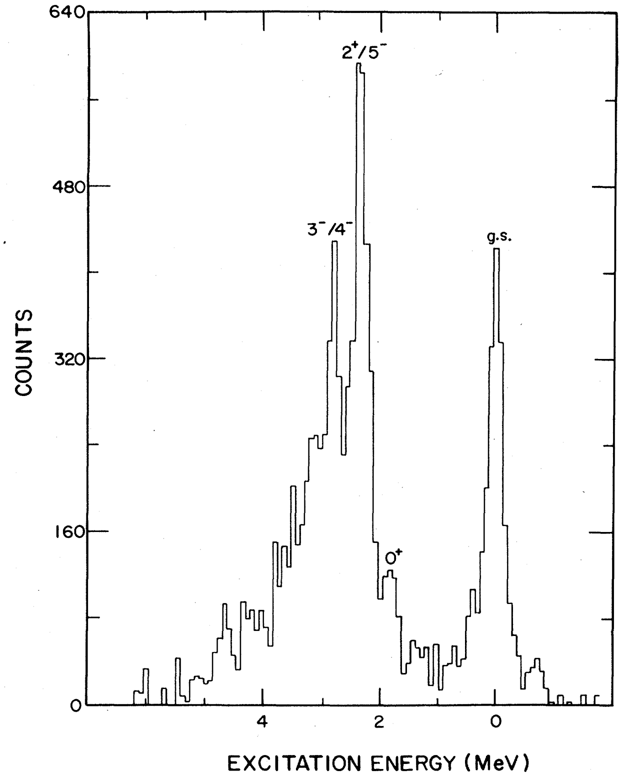

FIG. 8. Excitation spectrum of ^{90}Zr final nucleus in the reaction $^{91}\mathrm{Zr}+\mathrm{p}\rightarrow{}^{90}\mathrm{Zr}+\mathrm{p}+\mathrm{n}$ at 16.0 MeV incident energy. This is the projection of Fig. 6 on an axis perpendicular to the E_{n} versus E_{p} straight bands.

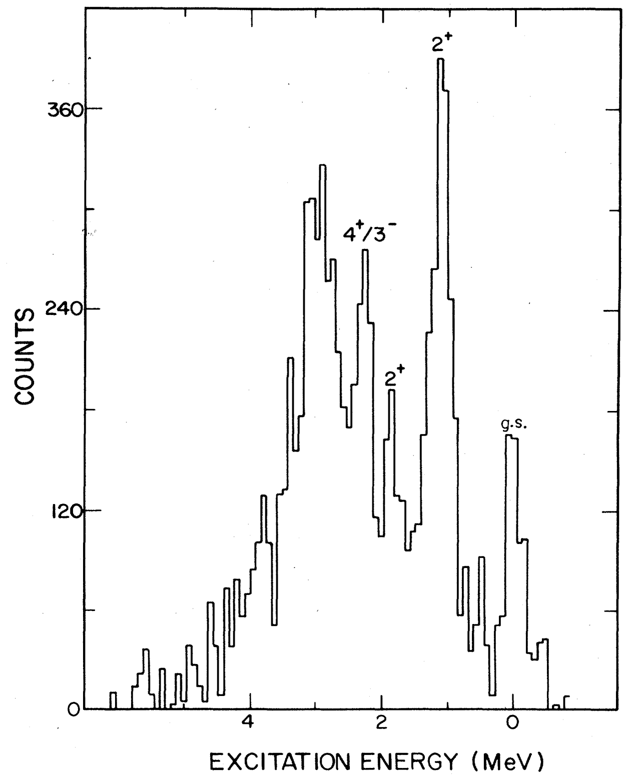

FIG. 9. Excitation spectrum of ^{86}Sr final nucleus in $^{87}\mathrm{Sr}+\mathrm{p}\rightarrow{}^{86}\mathrm{Sr}+\mathrm{p}+\mathrm{n}$ reaction at 16.7 MeV incident energy.

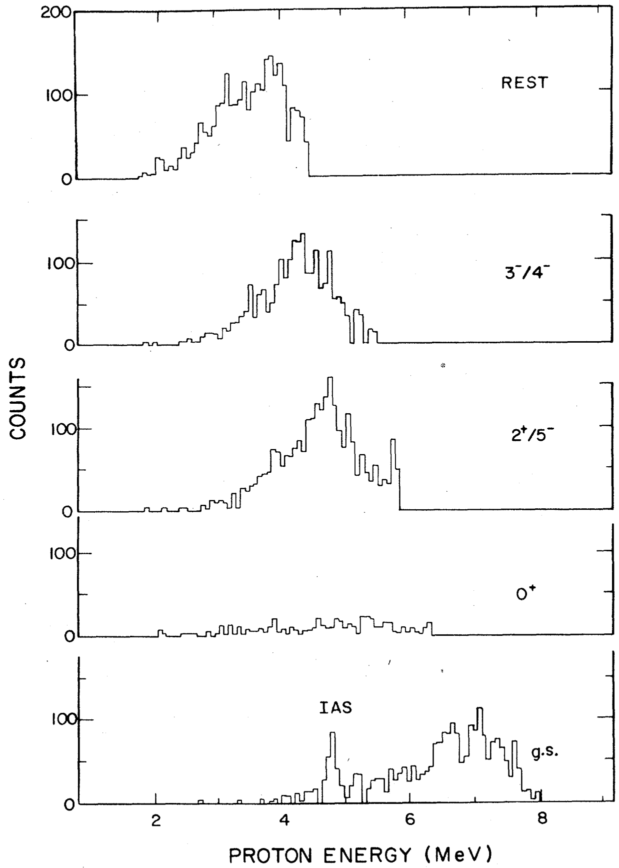

FIG. 10. Energy distribution of the outgoing protons in the ^{91}Zr(p,pn + np)^{90}Zr reactions at 16.0 MeV incident energy for the ground state and some obvious excited states of ^{90}Zr final nucleus. The peak appearing at 4.7 MeV in the ground state plot is due to the proton decay of the isobaric analog state of ^{91}Zr in ^{91}Nb.

tion in the scattering chamber wall, N_{el} is the number of protons elastically scattered by the target, into the proton counter, Ω_{n} is the solid angle of the neutron detector, and $d\sigma/d\Omega_{\text{el}}$ is the proton elastic differential cross section for the corresponding target and incident energy. These elastic differential cross sections were measured in separate experiments.

The above analysis was applied to data obtained at 15.0, 16.0, and 16.7 MeV for ^{87}Sr and at 16.0 and 17.0 MeV for ^{91}Zr. In an earlier experiment, data were also obtained at 16.0 and 17.6 MeV for ^{87}Sr and at 14.0, 16.0, and 17.6 MeV for ^{91}Zr. These early data were not complete; we recorded histograms rather than event data and a good time-of-flight calibration is absent. In these cases, total cross sections were extracted by normalizing to the histogram data at 16.0 MeV, and using the value measured in subsequent event-mode experiments for the cross section at this energy.

Isobaric analog states (IAS's) could contribute to the (p,np) cross sections by both direct and statistical processes. The direct charge exchange (p,n) reaction can excite the analog of the ground state of the target, which can subsequently emit a proton. We see a peak in the ^{91}Zr(p,np) spectra due to this mechanism (see Figs. 3, 6, and 10), but none in the ^{87}Sr data. The peak in the zirconium data was subtracted before the Hauser-Feshbach analysis. Analog states could effect the statistical decay of the compound systems if (p,n) or (p,nγ) reactions populate compound nuclear states whose proton widths are enhanced by mixing with the analogs. The analog might subsequently have an enhanced probability for emission of a proton, rather than another low-energy gamma ray emission. Such processes would produce larger than usual numbers of protons of a given energy for all neutron energies, giving rise to bands of events of constant proton energy in plots such as Fig. 6. Such bands are not seen in the data, aside from the contributions of accidental coincidences; we conclude that the contribution of such processes to the cross sections of interest is negligible for the targets studied, even though the analogs of low-lying states of ^{87}Sr should fall within the proton window.[11]

IV. RESULTS

In this experiment, neutron-proton coincidences were measured following proton bombardment, thus giving the cross sections for the composite reactions (p,pn + np) as shown in Fig. 1. The threshold for detecting neutrons in

TABLE I. Differential cross sections for the ^{91}Zr(p,pn + np)^{90}Zr reactions at $E_{\text{p}} = 16.0$ MeV. (Excitation energies in MeV.)

	Det. 1 (100°)	Det. 2 (65°)	Mean value
$\left[\frac{d\sigma}{d\Omega}\right]_{\text{pn+np}}$ (mb/sr)	39.6 ±4.6	46.0 ±5.3	42.8 ±3.5
σ_{rel} (%)	25.6 ±1.5	12.2 ±1.8	14.0 ±1.3
$\sigma_{\text{rel}}(0^+;E_x=1.7)$ (%)	2.6 ±0.8	4.6 ±0.9	3.6 ±0.6
$\sigma_{\text{rel}}(2^+,5;E_x\cong 2.3)$ (%)	35.8 ±3.2	34.3 ±3.2	35.0 ±2.3
$\sigma_{\text{rel}}(3^-,4^-;E_x\cong 2.7)$ (%)	17.9 ±1.8	15.7 ±1.6	16.8 ±1.2
σ_{rel}(Rest) (%)	18.1 ±2.0	24.3 ±2.9	21.3 ±1.8
$\left[\frac{d\sigma}{d\Omega}\right]_{\text{elast}}$ (mb/sr)			3.36±0.12
$\left[\frac{d\sigma}{d\Omega}\right]_{\text{IAS}}$ (mb/sr)	0.47±0.07	1.25±0.20	

TABLE II. Differential cross sections for the ^{91}Zr(p,pn + np)^{90}Zr reactions at $E_p = 17.0$ MeV. (Excitation energies in MeV.)

	Det. 1 (100°)	Det. 2 (65°)	Mean value
$\left[\frac{d\sigma}{d\Omega}\right]_{pn+np}$ (mb/sr)	34.5 ±4.6	40.0 ±6.0	37.3 ±3.8
σ_{rel} (%)	15.8 ±1.9	21.1 ±1.4	23.3 ±1.0
$\sigma_{rel}(0^+;E_x=1.7)$ (%)	5.3 ±1.4	4.0 ±1.5	4.6 ±1.0
$\sigma_{rel}(2^+,5^-;E_x\cong 2.3)$ (%)	33.4 ±5.3	28.3 ±7.4	30.9 ±4.6
$\sigma_{rel}(3^-,4;E_x\cong 2.7)$ (%)	14.7 ±2.3	20.5 ±3.3	17.6 ±2.0
σ_{rel}(Rest) (%)	30.8 ±4.8	35.0 ±7.1	32.9 ±4.3
$\left[\frac{d\sigma}{d\Omega}\right]_{elast}$ (mb/sr)			2.02±0.10
$\left[\frac{d\sigma}{d\Omega}\right]_{IAS}$ (mb/sr)	0.65±0.25	1.16±0.45	

the two detectors was set by software at 600 keV, and thus neutrons below that energy are not included in the present results. The threshold for protons in the ΔE-E telescope was set near 1.8 MeV, but this value is sufficiently below the Coulomb barrier that essentially no protons were missed from the targets of interest.

The differential cross sections for the composite reactions (p,pn + np) are given in Tables I and II for the ^{91}Zr target and Tables III—V for the ^{87}Sr target. Separate cross sections are shown corresponding to the two neutron detectors at 65° and 100° with the proton detector fixed at 135°. Partial cross sections for populating various final states in ^{90}Zr and ^{86}Sr are shown as percentages of the differential cross section at each neutron angle. The tables also contain the 135° proton elastic scattering cross sections measured at each energy and used to normalize the reaction cross sections. As mentioned in the preceding section, the reaction ^{91}Zr(p,n$\tilde{\rm p}$) to the ground state of ^{90}Zr through the isobaric analog state in ^{91}Nb was observed, and can be compared with other measurements.[12–14] Multiplying our 16 MeV (p,n$\tilde{\rm p}$) differential cross sections by 4π (Table I) gives 5.9 mb at $\theta = 100°$ and 15.7 mb at $\theta_n = 65°$. Similarly, at 17 MeV incident energy (Table II), the (p,n$\tilde{\rm p}$) cross sections are 8.2 and 14.6 mb. These values are in satisfactory agreement with the data of Refs. 12—14. Also, the factor of about 2 increases from $\theta_n = 100°$ to 65°, which reflects the forward peaking of the (p,n) reaction, is in good agreement with the calculations of Madsen.[15]

In contrast to the IAS contributions, the principal (p,pn + np) reactions show, within the errors, no angular variation between the two observed angles for neutron detection. Hence, the results were averaged and multiplied by 4π to obtain the total cross sections shown in Figs. 11 and 12. Figures 13 and 14 display cross sections with results from both pn and np emission for different final states of the ^{86}Sr and ^{90}Zr nuclei. An experiment similar to this one[16] surveyed (p,pn + np) reactions on 12 different nuclei. Although no cross sections are given in Ref. 16, we can compare cross section ratios to separate final states of ^{90}Zr, as shown in Fig. 14. Our 17 MeV data give a ratio of 0.33±0.08 between the cross sections leading to the 1.7 MeV state and the ground state of ^{90}Zr, compared to a value of 0.21 extracted from the work of Ref. 16. Similarly, the ratio of the summed cross sections leading to the next four states (2.16, 2.32, 2.74, and 2.75 MeV) over the ground state gives 3.5±0.9, compared to a value of 2.1 in the work of Ref. 16.

TABLE III. Differential cross sections for the ^{87}Sr(p,pn + np)^{86}Sr reactions at $E_p = 15.0$ MeV. (Excitation energies in MeV.)

	Det. 1 (100°)	Det. 2 (65°)	Mean value
$\left[\frac{d\sigma}{d\Omega}\right]_{pn+np}$ (mb/sr)	5.52±0.81	7.21±1.12	6.37±0.69
σ_{rel}(g.s.) (%)	25.5 ±3.3	18.2 ±3.0	21.9 ±2.2
$\sigma_{rel}(2^+;E_x=1.08)$ (%)	40.2 ±4.3	39.4 ±5.3	39.8 ±3.4
$\sigma_{rel}(2^+;E_x=1.85)$ (%)	10.2 ±2.0	8.3 ±1.1	9.2 ±1.1
$\sigma_{rel}(4^+,3^-;E_x\cong 2.35)$ (%)	12.1 ±3.8	21.9 ±5.1	17.0 ±3.2
σ_{rel}(Rest) (%)	12.0 ±4.5	12.2 ±5.9	12.1 ±3.7
$\left[\frac{d\sigma}{d\Omega}\right]_{elast}$ (mb/sr)			3.45±0.27

TABLE IV. Differential cross sections for the ^{87}Sr(p,pn + np)^{86}Sr reactions at $E_p = 16.0$ MeV. (Excitation energies in MeV.)

	Det. 1 (100°)	Det. 2 (65°)	Mean value
$\left[\frac{d\sigma}{d\Omega}\right]_{pn+np}$ (mb/sr)	13.6±2.1	16.9±2.5	15.3 ±1.6
σ_{rel}(g.s.) (%)	18.0±3.6	17.5±3.2	17.8 ±2.4
$\sigma_{rel}(2^+;E_x=1.08)$ (%)	26.0±4.4	28.7±4.1	27.3 ±3.0
$\sigma_{rel}(2^+;E_x=1.85)$ (%)	14.8±4.0	9.2±3.6	12.0 ±2.7
$\sigma_{rel}(4^+,3^-;E_x\cong 2.35)$ (%)	16.2±5.2	22.9±6.1	19.6 ±4.0
σ_{rel}(Rest) (%)	25.0±7.0	23.3±4.6	21.7 ±6.0
$\left[\frac{d\sigma}{d\Omega}\right]_{elast}$ (mb/sr)			2.82±0.16

V. COMPARISON WITH THEORETICAL PREDICTIONS

A reaction model that combines multistep Hauser-Feshbach and preequilibrium calculations[17] was used to provide theoretical predictions of (p,np + pn) cross sections. The reaction sequence included not only these channels but competing ones such as (p,p′), (p,n), (p,pγ), (p,nγ), (p,α), and (p,2n). Each nucleus appearing in a reaction sequence was described using discrete level data[18] available at low excitation energies, while at higher excitations a continuum representation was employed that included nuclear level densities based on the Gilbert-Cameron formalism.[19]

Expressions have been developed[17] to calculate the population of discrete levels for continuum energy bins for a given residual or compound nucleus. The population of continuum energy bins $P^{(n+1)}(UJ\Pi)$ in the $(n+1)$st compound system formed by particle disintegration of the nth compound nucleus is given by

$$P^{(n+1)}(UJ\Pi)=\int dU' \sum_{J'\Pi'} \hat{P}^{(n)}(U'J'\Pi')\frac{\Gamma_a^{(n)}(U'J'\Pi',UJ\Pi)}{\Gamma(U'J'\Pi)}\rho^{(n+1)}(UJ\Pi)\ . \tag{1a}$$

Here $\hat{P}^{(n)}(U'J'\Pi')$ is the population of continuum energy bins in the nth system after gamma-ray cascades have been considered, U is the excitation energy, ρ is the level density, and a defines the type of particle emitted. The population of the first compound system is determined from its formation cross section resulting from a sum over transmission coefficients evaluated at the c.m. energy of the incident proton. The partial decay widths appearing in Eq. (1) have the form

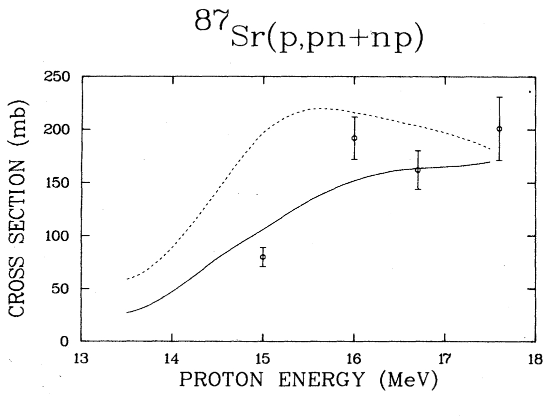

FIG. 11. Excitation function for ^{87}Sr(p,pn + np). The points are the present data. The solid line is the multistep statistical model calculations with the parameters described in the text and including a neutron energy threshold of 0.6 MeV. The dashed curve is the same calculation ignoring this threshold.

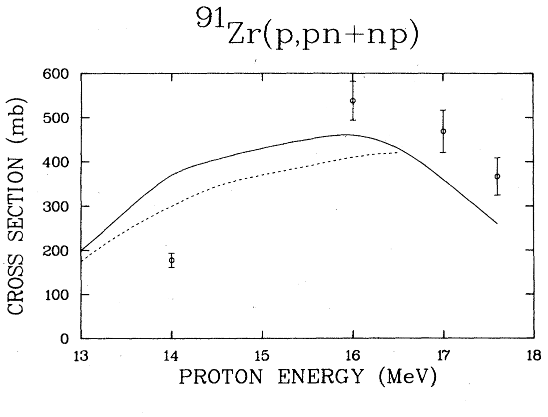

FIG. 12. Excitation function for ^{91}Zr(p,pn + np). The points are the present data. The solid line is the multistep statistical model calculation with the parameters of Ref. 25. The dashed curve shows the effect of increasing the γ-ray strength function by a factor of 2.

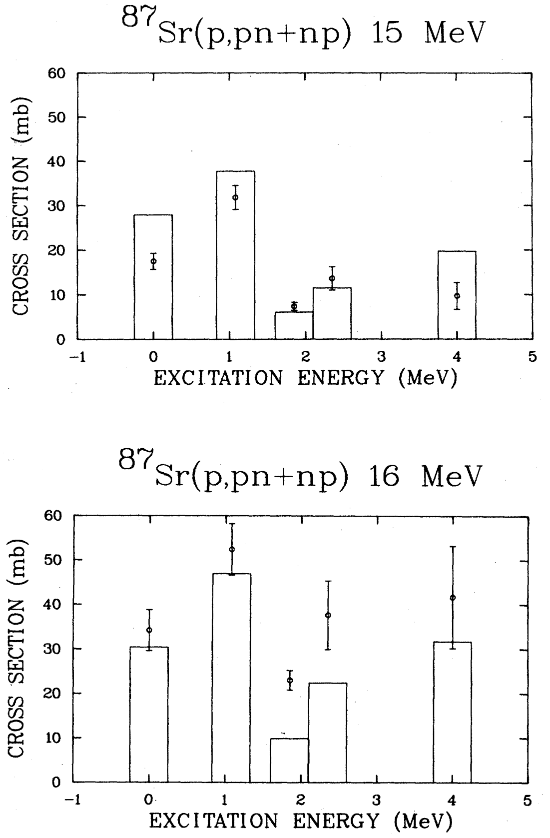

FIG. 13. Cross sections for particular final states in the reaction ^{87}Sr(p,pn + np)^{86}Sr at 15 (a) and 16 (b) MeV incident proton energy. The histogram shows the theoretical predictions.

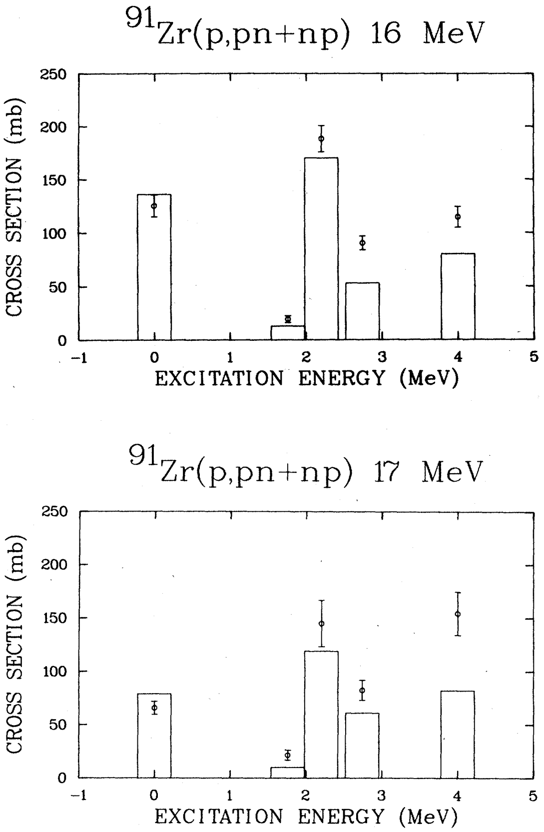

FIG. 14. Same as Fig. 13 for ^{91}Zr(p,pn + np)^{90}Zr except 16 (a) and 17 (b) MeV.

$$\Gamma_a^{(n)}(U'J'\Pi',UJ\Pi) = \frac{1}{2\pi\rho(U'J'\Pi')}\sum_s\sum_l T_l(U'-U-B_a) \ , \qquad \text{(1b)}$$

where B_a is the binding energy of the emitted particle. The transmission coefficients T_l appearing in this equation are obtained using optical model potentials for neutrons, protons, and alpha particles; some of these will be described later. Continuum gamma-ray transitions also involve transmission coefficients appropriate to the multipolarity involved (in this calculation $E1$, $M1$, and $E2$) that are based on empirically determined gamma-ray strength functions.

For the population of discrete levels, an equation similar to Eq. (1) holds, so that

$$P^{(n+1)}(E_iJ_i\Pi_i)=\int dU' \sum_{J'\Pi'} \hat{P}^{(n)}(U'J'\Pi') \times\frac{\Gamma_a^{(n)}(U'J'\Pi',E_iJ_i\Pi_i)}{\Gamma(U'J'\Pi')} \ , \qquad \text{(2a)}$$

where i refers to a specific discrete level. The partial width for continuum to discrete level transitions then has the form

$$\Gamma_a(U'J'\Pi',E_iJ_i\Pi_i)=\sum_s\sum_l T_l(U'-E_i-B_a) \ . \qquad \text{(2b)}$$

The total width Γ appearing in the denominators of Eqs. (1) and (2) is obtained by summing over the appropriate partial widths for continuum bins or discrete levels associated with each channel a.

The portion of the calculation that determined the population of the second compound nucleus formed by particle emission from the first included preequilibrium corrections based on the exciton model of Kalbach.[20] The calculation of preequilibrium corrections involved determining rates for creation or destruction of particle-hole pairs as well as the probability for particle emission. These rates (see Ref. 20) are proportional to the square of the average matrix element, $|M|^2$, for the effective residual two-body interaction. Within the Kalbach formalism this quantity is determined empirically and is assumed to be dependent both on excitation energy and exciton number.[21] The normalization constant used for $|M|^2$ throughout our calculations was 160 MeV.[3]

An aspect of Hauser-Feshbach theory that we did not include was consideration of the role of isospin in statistical reaction processes.[22] For proton-induced reactions, one expects an enhancement of the proton emission proba-

TABLE V. Differential cross sections for the ^{87}Sr(p,pn + np)^{86}Sr reactions at $E_p = 16.7$ MeV. (Excitation energies in MeV.)

	Det. 1 (100°)	Det. 2 (65°)	Mean value
$\left[\frac{d\sigma}{d\Omega}\right]_{\text{pn+np}}$ (mb/sr)	11.2±1.6	14.6±2.2	12.9 ±1.4
σ_{rel}(g.s.) (%)	11.5±1.3	9.9±1.4	10.7 ±1.0
$\sigma_{\text{rel}}(2^+;E_x=1.08)$ (%)	27.1±2.6	24.6±2.7	25.9 ±1.9
$\sigma_{\text{rel}}(2^+;E_x=1.85)$ (%)	8.5±1.3	9.9±1.7	9.2 ±1.1
$\sigma_{\text{rel}}(4^+,3^-;E_x\cong 2.35)$ (%)	12.6±2.8	13.3±4.1	12.9 ±2.5
σ_{rel}(Rest) (%)	40.3±6.2	42.3±8.4	41.3 ±5.2
$\left[\frac{d\sigma}{d\Omega}\right]_{\text{elast}}$ (mb/sr)			2.39±0.18

bility because of the population of upper isospin states, $T^>$. However, such effects are lessened by mixing of upper isospin into lower isospin states. This, coupled with the fact that isospin effects enhance competing (p,p′) channels directly, rather than the (p,np) and (p,pn) reactions of interest here, led us to ignore it in our Hauser-Feshbach calculations. Since completion of our calculations preliminary cross sections obtained using methods similar to those described here, but including isospin effects, have been completed by Gardner and Gardner[23] for p + ^{93}Nb and p + ^{87}Sr reactions. They found differences of 10% or less in calculated (p,n) and (p,np + pn) cross sections between the case of full isospin conservation and complete isospin damping.

A major emphasis of our calculation was assessment of the ability of these reaction models to reproduce (p,np + pn) data measured in this experiment while providing a consistent theoretical linkage to complementary experimental results. For this reason we chose not to employ global input parameters or systematics but instead optimized model parameters based on an analysis of information available from a variety of independent data sources. As noted in the Introduction, the proximity of these nuclei to two-shell closures introduces conditions not routinely encountered in such calculations. The existence of the proton window in ^{87}Y and ^{91}Nb (see Fig. 1), where only proton and gamma-ray emission are energetically allowed, provides conditions under which the sub-Coulomb barrier behavior of the proton optical model can be tested. Such data are complementary to information obtained from low energy (p,n) measurements although in this case the spectrum of compound nuclear states involved is more complicated because of the multistep nature of the reaction. In addition, the balance between proton and gamma-ray emission encountered in this situation places rather stringent demands upon the parametrization of the gamma-ray strength function.

We began our parameter analysis with the optical model, gamma-ray strength functions, and level density parameters detailed in Ref. 24, because similar techniques were used there for parameter determination. We adjusted the neutron optical parameters to reproduce new resonance data available since this 1979 study, while maintaining reasonable fits to neutron total and elastic scattering data. The set of revised neutron optical parameters appears in Table VI along with a comparison to recent neutron resonance data[25] from n + ^{89}Y reactions.

The proton optical parameters of Ref. 24 were further adjusted to reproduce new sub-Coulomb barrier (p,n) data[26] for ^{87}Sr between 3 and 6 MeV. In addition, the parameters were constrained to produce reaction cross sections comparable to results from global parameter sets[27,28] at higher incident energies. The optical parameters derived in this manner appear in Table VII, and Fig. 15 compares the ratio of reaction cross sections calculated using the Perey[27] and Becchetti-Greenlees parameters[28] with results using our parameters. Substantial differences occur in the sub-Coulomb energy region of interest to our calculations.

Our determination of gamma-ray strength functions was based on use of the equation[25]

$$\frac{\langle \Gamma_\gamma \rangle}{\langle D \rangle} = \int_0^{B_n} f \epsilon_\gamma^3 \rho(B_n - \epsilon_\gamma) d\epsilon_\gamma \,, \tag{3a}$$

where f represents the strength function, including in our

TABLE VI. The neutron optical model parameters [a] used for n + ^{87,88}Y calculations.

	r	a
$V = 49.8 - 0.28E$	1.24	0.62
$V_{\text{SO}} = 6.2$	1.12	0.47
$W_{\text{VOL}} = -2.7 + 0.3E^{\text{b}}$	1.24	0.66
$W_{\text{SD}} = 2 + 0.3E$	1.24	0.58
Above 15 MeV		
$W_{\text{SD}} = 6.5$		

Comparison to neutron strength functions

	Experimental (Ref. 26)	Theoretical
S_0 ($\times 10^{-4}$)	0.27±0.05	0.33
S_1 ($\times 10^{-4}$)	2.65±0.3	3.75
R' (fm)	6.7±0.1	6.55

[a] All well depths are in MeV; geometrical parameters are in fm.

[b] Or zero, whichever is greater.

TABLE VII. The proton optical model parameters[a] used for p + ^{87}Sr calculations.

	r	a
$V\ \ =62.8-0.32E$	1.2	0.73
$V_{SO}=\ 6.4$	1.03	0.63
$W_{SD}=\ 3.5+0.5E$	1.3	0.4
$r_c\ \ =\ 1.2$		

[a]Well depths are in MeV; geometrical parameters are in fm.

case $E1$, $M1$, and $E2$ contributions; B_n is the neutron binding energy; and $\langle \Gamma_\gamma \rangle$ and $\langle D \rangle$ are the average gamma-ray width and spacing for s-wave neutron resonances. To represent the $E1$ strength function, we chose a giant dipole resonance (GDR) form

$$f_{E1}=\frac{K\epsilon_\gamma \Gamma_{\rm GDR}}{(\epsilon_\gamma \Gamma_{\rm GDR})^2+(\epsilon_\gamma^2-E_{\rm GDR}^2)^2}\ , \tag{3b}$$

where the normalization constant was determined by fitting neutron capture data in this mass region. Strength functions for $M1$ and $E2$ multipolarities were assumed to be constant, and were normalized to the $E1$ contributions using systematics for relative $M1$ and $E2$ strengths.[29] For our p + ^{87}Sr calculations, we determined the strength function for the ^{87}Y compound system by analysis of ^{86}Sr(p,γ) data.[26]

As described earlier the excitation model was used to correct populations in the second compound systems for preequilibrium particle emission. The importance of these corrections increases at the higher incident energies of this calculation, although in all cases considered here, substantial preequilibrium emission (up to 50 percent) was computed for (p,p) reactions. The presence of such preequilibrium corrections hardened the calculated proton emission spectrum (relative to that determined from consideration of statistical processes alone). Thus the probability for inelastic proton scattering is increased while that for the (p,p'n) reaction (one of the two processes of interest here) is decreased. In contrast, the fraction of preequilibrium neutron emission was calculated to be significantly smaller (~ 10 percent) so that the effect of such nonstatistical processes on the (p,np) reaction was small. Since, we will discuss later, (p,np) processes appear to be the dominant portion of the coincident n-p emission reactions of interest in this experiment, overall preequilibrium effects are not major, but do increase as one goes to higher incident energies.

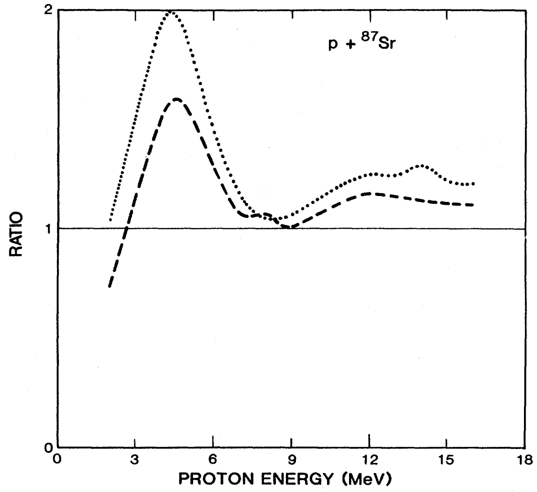

FIG. 15. The ratio of p + ^{87}Sr reaction cross sections calculated using Perey and Becchetti-Greenlees proton optical parameters (dashed and dotted curves) to results obtained with the parameters of Table VII.

The solid curve appearing in Fig. 11 represents our calculated cross sections for ^{87}Sr(p,np + pn) reactions. In addition to use of the optical model and strength function parameters described above, we adjusted the Fermi-gas level-density parameter for ^{87}Y upward by about 6% over the value from the Cook systematics,[30] in order to improve agreement with the data. Because the experiment involved an energy threshold of 0.6 MeV for the neutron detector used in the coincidence measurements, we included a similar energy cutoff there. The dashed curve shown illustrates the cross sections obtained when this threshold is ignored. Because of the large proton window existing in the ^{87}Y compound nucleus, most of the calculated cross section of Fig. 11 results from the (p,np) reaction, as illustrated in Fig. 16.

We also obtained theoretical cross sections for the population of discrete levels in the residual ^{86}Sr nucleus via these reaction paths. This experiment is unique in providing tests of multistep Hauser-Feshbach calculations leading to discrete final levels rather than the continuum. Figures 13(a) and (b) indicate the good agreement obtained between the data and calculations at incident proton ener-

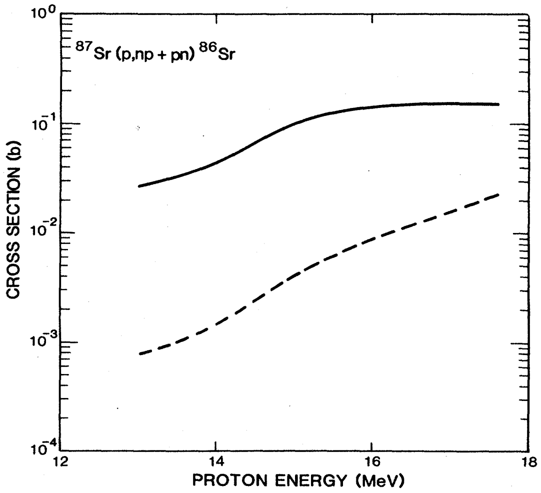

FIG. 16. Relative yields of ^{87}Sr(p,np) (solid curve) and ^{87}Sr(p,pn) (dashed curve) reaction paths corresponding to the calculation of Fig. 13.

gies of 15 and 16 MeV. In addition, we have reproduced data[26] available for the competing ^{87}Sr(p,n) and ^{87}Sr(p,2n) channels. Thus, within a consistent theoretical framework employing parameters determined from independent data, we have demonstrated the ability to analyze the major reaction channels of the p + ^{87}Sr system.

We performed similar calculations for ^{91}Zr(p,np + pn) reactions, but without suitable experimental data to determine the parameters directly. We therefore used the parameters of Ref. 24 obtained by analysis of neutron and proton reaction data on yttrium and zirconium isotopes. Figure 12 compares our calculated ^{91}Zr(p,np + pn) values with results from this experiment. At approximately 16—17 MeV, the agreement is reasonable, although there is a significant overprediction of the data at lower incident energies. Attempts to make *ad hoc* adjustments of parameters were not successful in simultaneously reproducing the overall shape and magnitude of the experimental data. The dashed curve in Fig. 12 illustrates the effect of increasing the gamma-ray strength function of ^{91}Nb by a factor of 2. Discrete level populations in the ^{90}Zr residual nucleus were also computed and are compared with the present data at $E_p = 16$ and 17 MeV in Figs. 15(a) and (b). Again, the agreement is good, particularly considering difficulties resulting from the multistep nature of the problem and the range of discrete level spins (0^+, 2^+, 5^-, 4^-, and 3^-).

These comparisons have illustrated the ability of the multistep Hauser-Feshbach models (coupled with preequilibrium corrections) to describe the reaction mechanism governing (p,np + pn) processes. This conclusion is in contrast to that of Ref. 16 where the use of crude models and parameters led to postulation of direction reaction processes as the dominant reaction mechanism. A principle reason for our success in reproducing these data is the methodology used in parameter determination, particularly regarding constraints introduced by analysis of independent data.

VI. CONCLUSION

The $^{87}\mathrm{Sr} + \mathrm{p} \rightarrow {}^{86}\mathrm{Sr} + \mathrm{pn}$ and $^{91}\mathrm{Zr} + \mathrm{p} \rightarrow {}^{90}\mathrm{Zr} + \mathrm{pn}$ cross sections were measured with incident proton energies that populate the compound nuclei ^{88}Y* and ^{92}Nb* at the same excitation energy as the reactions induced by 14 MeV neutrons on ^{87}Y and ^{91}Nb. A comparison of the data with calculations based on a multistep statistical model shows substantial agreement. The calculations can therefore be used with reasonable confidence to predict cross sections for unstable target nuclei.

ACKNOWLEDGMENTS

This work was supported by the U.S. Department of Energy. One of us (J.C.D.) extends his thanks to the Swiss National Foundation for Scientific Research that supported him with a research grant during a one year stay at the Los Alamos National Laboratory.

---

[1] S. M. Grimes, R. C. Haight, K. R. Alvar, H. H. Barschall, and R. R. Borchers, Phys. Rev. C **19**, 2127 (1979).

[2] S. M. Grimes, R. C. Haight, and J. D. Anderson, Nucl. Sci. Eng. **62**, 187 (1977).

[3] S. M. Grimes, R. C. Haight, and J. D. Anderson, Phys. Rev. C **17**, 508 (1978).

[4] R. C. Haight, S. M. Grimes, R. G. Johnson, and H. H. Barschall, Phys. Rev. C **23**, 700 (1981).

[5] R. J. Prestwood, Kimberly W. Thomas, David R. Nethaway, and Norman L. Smith, Phys. Rev. C **29**, 805 (1984).

[6] C. H. Johnson, A. Galonsky, and R. L. Kernell, Phys. Rev. C **20**, 2052 (1979).

[7] D. S. Flynn, R. L. Hershberger, and F. Gabbard, Phys. Rev. C **26**, 1744 (1982).

[8] J. B. Wilhelmy (private communication); see also Ref. 26.

[9] V. V. Verbinski, W. R. Burrus, T. A. Love, W. Zobel, N. W. Hill, and R. Textor, Nucl. Instrum. Methods **65**, 8 (1968).

[10] M. Drosg, Nucl. Sci. Eng. **67**, 190 (1978).

[11] F. Meuders, W. P. T. M. Van Eegham, and P. Spilling, Nucl. Phys. **A196**, 353 (1972).

[12] A. I. Yavin, R. A. Hoffswell, L. H. Jones, and T. M. Mowein, Phys. Rev. Lett. **16**, 1049 (1966).

[13] J. P. Bondorf, C. Ellegaard, J. Kantele, H. Lütken, and P. Vedelsby, Nucl. Phys. **A101**, 338 (1967).

[14] P. S. Miller and G. T. Garvey, Nucl. Phys. **A163**, 65 (1971).

[15] V. A. Madsen, in *Proceedings of the Conference on Nuclear Isospin, Asilomar, 1969*, edited by I. D. Anderson, S. D. Bloom, J. Cerny, and W. W. True (Academic, New York, 1969); p. 149.

[16] B. L. Cohen, C. L. Fink, J. C. van der Weerd, and R. J. Petty, Phys. Rev. C **1**, 1237 (1970).

[17] P. G. Young and E. D. Arthur, Los Alamos Scientific Laboratory Report No. LA-6947, 1977.

[18] *Table of Isotopes*, 7th ed., edited by C. Michael Lederer and Virginia S. Shirley (Wiley, New York, 1978).

[19] A. Gilbert and A. G. W. Cameron, Can. J. Phys. **43**, 1446 (1965).

[20] C. Kalbach Z. Phys. A **283**, 401 (1977).

[21] C. Kalbach, Z. Phys. A **287**, 319 (1978).

[22] S. M. Grimes, J. D. Anderson, A. K. Kerman, and C. Wong, Phys. Rev. C **5**, 85 (1972).

[23] D. G. Gardner and M. A. Gardner (private communication).

[24] E. D. Arthur, Nucl. Sci. Eng. **76**, 137 (1980).

[25] S. F. Mughabghab, M. Divadeenam, and N. E. Holden, *Neutron Cross Sections* (Academic, New York, 1981), Vol. I.

[26] D. W. Barr, S. A. Beatty, M. M. Fowler, J. S. Gilmore, R. J. Prestwood, E. N. Treher, and J. B. Wilhelmy, Los Alamos National Laboratory Report No. LA-9797-PR, 1983.

[27] F. G. Perey, Phys. Rev. **181**, 745 (1963).

[28] F. D. Becchetti and G. W. Greenlees, Phys. Rev. **182**, 1190 (1969).

[29] J. Kopecky, in *Proceedings of the Fourth International Conference* on *Neutron Capture Gamma-Ray Spectroscopy, Grenoble, 1981*, Conference Series No. 62, edited by T. von Egidy (Institute of Physics and Physical Society, London, 1981), p. 423.

[30] J. L. Cook, H. Ferguson, and A. R. de L. Musgrove, Aust. J. Phys. **20**, 477 (1967).